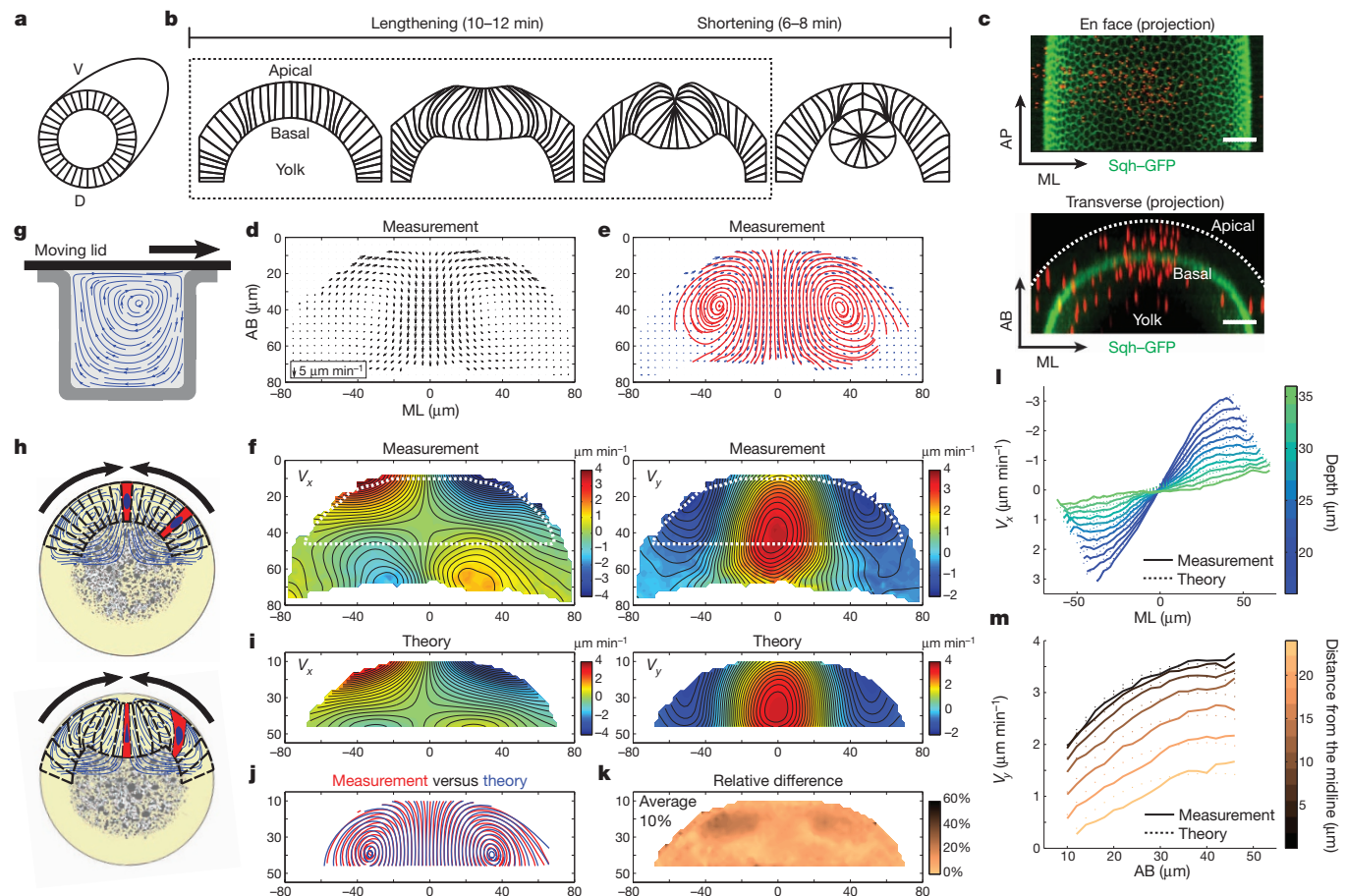


# Apical constriction drives tissue-scale hydrodynamic flow to mediate cell elongation

Bing He<sup>1\*</sup>, Konstantin Doubrovinski<sup>1\*</sup>, Oleg Polyakov<sup>2</sup> & Eric Wieschaus<sup>1,3</sup>

Epithelial folding mediated by apical constriction converts flat epithelial sheets into multilayered, complex tissue structures and is used throughout development in most animals<sup>1</sup>. Little is known, however, about how forces produced near the apical surface of the tissue are transmitted within individual cells to generate the global changes in cell shape that characterize tissue deformation. Here we apply particle tracking velocimetry in gastrulating *Drosophila* embryos to measure the movement of cytoplasm and plasma membrane during ventral furrow formation<sup>2,3</sup>. We find that cytoplasmic redistribution during the lengthening phase of ventral furrow formation can be precisely described by viscous flows that quantitatively match the

predictions of hydrodynamics. Cell membranes move with the ambient cytoplasm, with little resistance to, or driving force on, the flow. Strikingly, apical constriction produces similar flow patterns in mutant embryos that fail to form cells before gastrulation ('acellular' embryos), such that the global redistribution of cytoplasm mirrors the summed redistribution occurring in individual cells of wild-type embryos. Our results indicate that during the lengthening phase of ventral furrow formation, hydrodynamic behaviour of the cytoplasm provides the predominant mechanism transmitting apically generated forces deep into the tissue and that cell individualization is dispensable.



**Figure 1 | Cytoplasmic flow during ventral furrow formation.** **a, b,** Cross-section view of ventral furrow formation. V, ventral; D, dorsal. **c,** An embryo injected with fluorescent beads (red). Scale bar, 20 μm. AP, anterior-posterior; ML, medial-lateral; AB, apical-basal. **d, e,** The velocity field (arrows) and streamlines (red) of the cytoplasmic flow at  $t = 4\text{--}6\text{ min}$  ( $n = 14$  embryos). **f,** Heat maps of  $V_x$  and  $V_y$ , with smoothed contour lines of equal magnitude. Positive values indicate

left-to-right flow ( $V_x$ ) or basally directed flow ( $V_y$ ). The dotted line highlights the region subjected to theoretical comparison. **g,** A two-dimensional Stokes flow driven by a moving lid. **h,** Apical constriction drives cytoplasmic flow to mediate cell shape changes. **i,**  $V_x$  and  $V_y$  deduced from the Stokes equations. **j,** Streamlines of the measured (red) and deduced (blue) velocity fields. **k,** Relative difference in **j**. **l, m,**  $V_x$  (**l**) and  $V_y$  (**m**) as a function of ML or AB positions, respectively.

<sup>1</sup>Department of Molecular Biology, Princeton University, Princeton, New Jersey 08544, USA. <sup>2</sup>Department of Physics, Princeton University, Princeton, New Jersey 08544, USA. <sup>3</sup>Howard Hughes Medical Institute, Princeton University, Princeton, New Jersey 08544, USA.

\*These authors contributed equally to this work.

During *Drosophila* gastrulation, ventrally localized prospective mesoderm forms a furrow and invaginates from the surface of the embryo. As this furrow forms, individual cells first constrict at their apical end and undergo elongation ('cell lengthening'). During their subsequent invagination, cells shorten back to wedge-like shapes (Fig. 1a, b). Apical constriction is powered by an apically localized contractile actomyosin network that forms at the onset of gastrulation and is widely believed to be the main force driving ventral furrow formation<sup>4</sup>. Although it is unclear how stresses transmitted from the apical cortex mediate tissue movement in the interior of the embryo, a common view is that the cell surface and associated cytoskeleton play a major role in generating and transmitting forces within each cell, while the cytoplasm passively adopts the shape defined by the cortex. In an opposing view, the entire tissue is considered as a continuum; forces are transmitted continuously across the epithelium and its subdivision into cells is not a fundamental component in force transmission. Modelling studies have successfully described global tissue movements using both cell-based<sup>5–7</sup> and continuum viewpoints<sup>8–11</sup>. Although these studies identified plausible mechanisms that could mediate ventral furrow morphogenesis, the actual mechanism remains elusive. One fundamental limitation is that previous measurements of tissue deformation have an intrinsically limited spatial resolution of a single cell. A rigorous test of physical mechanisms, however, requires tissue deformation being tracked with subcellular resolution<sup>12</sup>.

With this goal in mind, we developed a strategy using injected sub-micrometre fluorescent beads as passive tracers to measure the motion of cytoplasm in *Drosophila* embryos<sup>13,14</sup> (Fig. 1c and Extended Data Fig. 1). The injected beads show extremely low mobility when there is no global movement of the tissue (Extended Data Fig. 2 and Supplementary Methods), thereby providing trackable landmarks for quantitative, high-resolution measurements of cytoplasmic flows (Extended Data Figs 3 and 4 and Supplementary Video 1). Figure 1d–f shows averaged two-dimensional velocity distribution and streamlines at a transverse cross section through the embryo at the middle of the lengthening phase ( $t = 4\text{--}6\text{ min}$ ; Supplementary Methods). The flow patterns do not change substantially during the lengthening phase (Extended Data Fig. 4a). When the shortening phase starts, the tracking of beads becomes difficult as beads locate deeper into the embryo. We therefore focused our analysis on the lengthening phase.

The measured movement of cytoplasm resembles a laminar flow (Fig. 1g) in that when the cortex constricts and moves, the underlying cytoplasm seems to be dragged with it (Fig. 1h). If this is in fact the case, tissue deformation in the interior of the embryo should follow the Stokes equations that describe the dynamics of viscous flows in the low Reynolds number regime. In particular, flow velocity at any point in the interior of an arbitrarily chosen domain will be uniquely determined by the velocity distribution at the domain boundaries. This allows for a quantitative and parameter-free comparison between Stokes dynamics and tissue movements (Methods). We found that the inferred velocity distribution is in close agreement with our measurements, with relative differences close to the measurement error ( $\sim 10\%$ ; Fig. 1i–m and Extended Data Fig. 4c). The close agreement strongly argues that tissue deformation during the lengthening phase could arise exclusively from the viscous response of the cytoplasm to the shear force generated by apical constriction at the cortex (Supplementary Notes).

This close agreement implies that lateral membranes do not exert appreciable forces on the cytoplasm and thus are expected to (1) co-move with the cytoplasmic flow and (2) be dispensable for the redistribution of the cytoplasm that underlies cell shape changes. We tested prediction 1 by tracking the movement of wheat germ agglutinin (WGA)-coated beads attached to the plasma membrane<sup>15</sup> (Fig. 2a, Extended Data Fig. 5 and Supplementary Videos 2 and 3). During gastrulation, the motion of such beads is very similar to non-WGA cytoplasmic beads, with a relative difference of only 20% at  $t = 5\text{ min}$  (Fig. 2b–d, Extended Data Fig. 6 and Supplementary Methods). Moreover, the flow of the WGA beads also matches the predictions of the Stokes equations with 86% similarity (Fig. 2f–i). Most interestingly, the expansion of the lateral

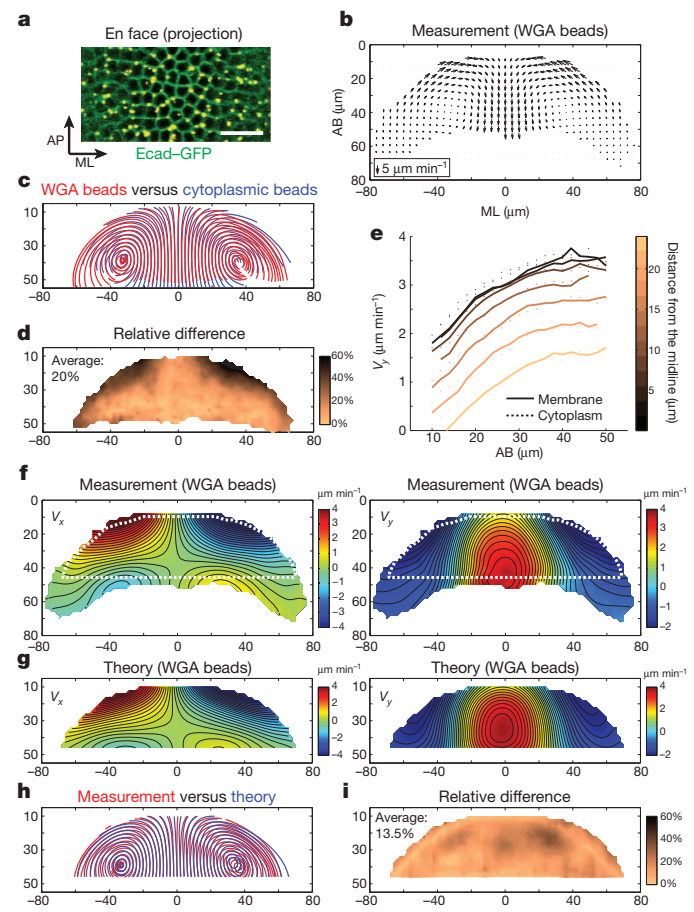


**Figure 2 | The movement and expansion of the lateral membranes follow the cytoplasmic flow.** **a**, Perivitelline injection of WGA-coated beads (yellow). Scale bar, 20  $\mu\text{m}$ . **b**, Velocity field of the WGA beads at  $t = 4\text{--}6\text{ min}$  ( $n = 10$  embryos). **c**, Streamlines of the WGA beads (red) and the cytoplasmic beads (blue). **d**, Relative difference in **c**. **e**,  $V_y$  as a function of AB positions. **f**, **g**, Heat maps of  $V_x$  and  $V_y$  of the WGA beads: **f**, measurement; **g**, theoretical prediction. **h**, Streamlines of the measured (red) and deduced (blue) velocity fields. **i**, Relative difference in **h**.

membranes closely matches the regional flow of the ambient cytoplasm, being highest apically and decreasing towards the base (Figs 1m and 2e). These data are very consistent with a model where lateral membranes extend passively as a consequence of the cytoplasmic flow without offering appreciable driving force or resistance.

To test prediction 2, we took advantage of the fact that *Drosophila* begins its development as a syncytium and only forms individual cells with basolateral membranes immediately preceding gastrulation. We have found that simultaneous elimination of two zygotically active genes (*CG9506* (*=slam*)<sup>16</sup> and *CG34137*) blocks the formation of basolateral membranes, while maintaining the normal subcellular organization of the cytoplasm (Fig. 3a, Extended Data Fig. 7 and Supplementary Videos 4, 5 and 7). In such embryos, the expression pattern of the mesoderm determinants *Twist* and *Snail*<sup>17</sup> is normal (Fig. 3c and Extended Data Fig. 8a), and gastrulation starts at the normal time, with myosin forming a cortical network that undergoes dynamic, pulsed contractions on the ventral surface (Supplementary Video 6 and Extended Data Fig. 8b, c). The average rate of the resultant apical constriction, however, is reduced to 60% of that in the wild type (Extended Data Fig. 9), presumably because the network is less well organized without cell individualization. As in wild-type embryos, apical constriction leads to formation of membrane blebs, albeit larger, on the ventral surface of the gastrulating acellular embryos<sup>3</sup> (Extended Data Fig. 8d).

Remarkably, apical constriction in the acellular embryos leads to basal movement of bulk cytoplasm and nuclei towards the yolk in a manner

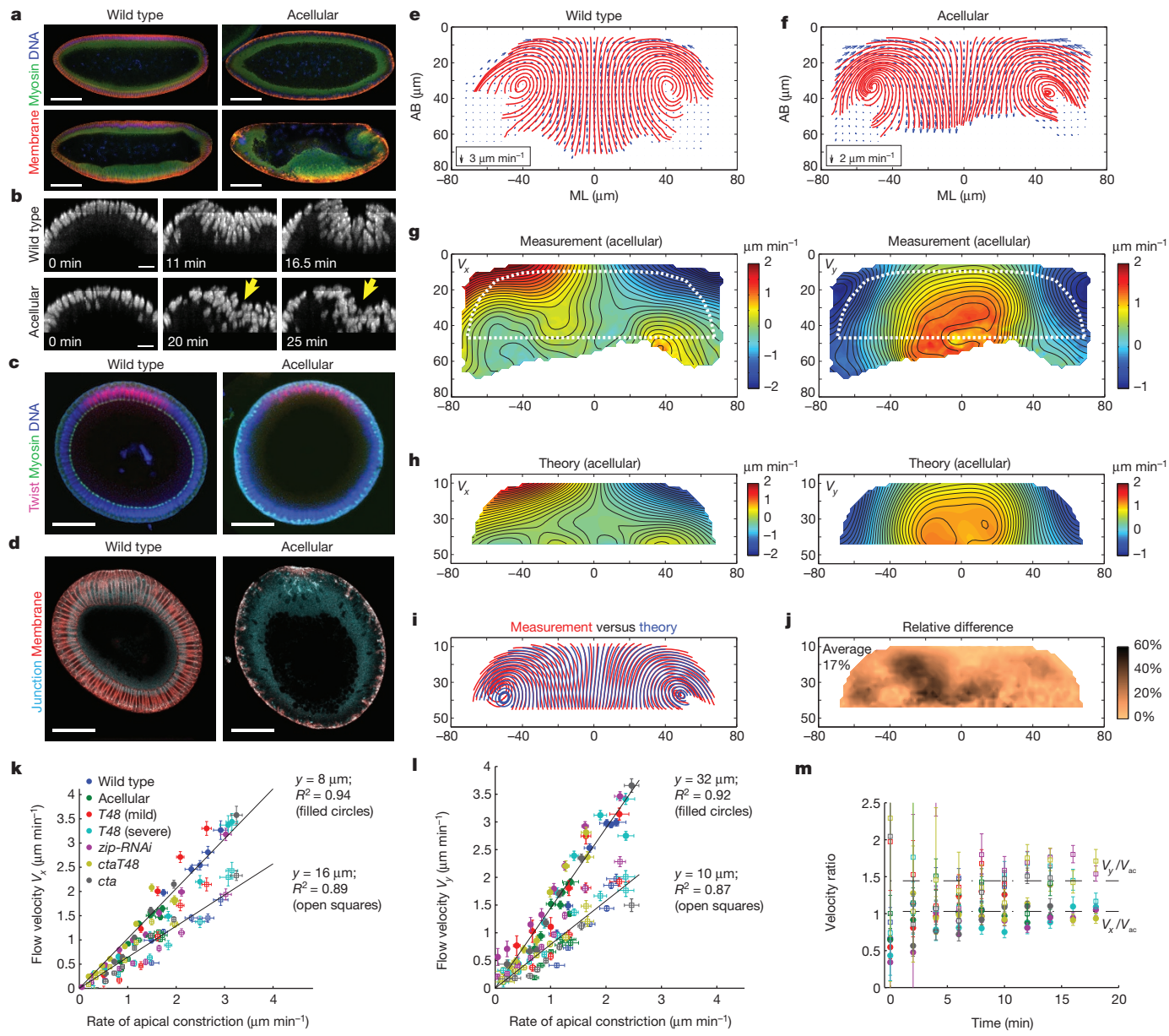


**Figure 3 | Apical constriction induces cytoplasmic flow independent of the basolateral membranes.** **a**, Midsagittal view of embryos showing membrane, myosin II and DNA. Top, cellularization; bottom, early gastrulation. Scale bars, 100  $\mu\text{m}$ . **b**, The nuclear movements during ventral furrow (arrows) formation. Scale bars, 20  $\mu\text{m}$ . **c**, Cross section of the embryos showing Twist, myosin II and DNA. Scale bars, 50  $\mu\text{m}$ . **d**, Cross section of early gastrulae showing membrane and adherens junctions. Scale bars, 50  $\mu\text{m}$ . **e, f**, The velocity field and streamlines of the cytoplasmic flow. Wild type,

$n = 20$  embryos; acellular,  $n = 18$  embryos. **g, h**, Heat maps of  $V_x$  and  $V_y$  in the acellular embryos: **g**, measurement; **h**, theoretical prediction. **i**, Streamlines of the measured (red) and deduced (blue) velocity fields. **j**, Relative difference in **i**. **k**,  $V_x$  as a function of the rate of apical constriction ( $V_{ac}$ ). **l**, Average  $V_y$  as a function of average  $V_{ac}$ . **m**,  $V_x/V_{ac}$  (filled circles) and  $V_y/V_{ac}$  (open squares) over time. Colour-coding is identical in **k–m**. Dashed lines, the best fit of the ratio. Error bars, s.e.m. in **k–m**.

similar to the wild type (Fig. 3b, d and Supplementary Video 7). The pattern of the cytoplasmic flow closely resembles that in the wild type, albeit with reduced velocity (Fig. 3e, f and Supplementary Video 8). Crucially, the reduced flow velocity quantitatively corresponds to the reduced rate of apical constriction (Extended Data Fig. 9i–k). Therefore, removing the basolateral membranes does not affect the physical response of the interior tissue to apical constriction, in strong confirmation of our model. As an extra control, we analysed four mutants that specifically affect the rate of apical constriction in otherwise normally cellularized embryos and found that in all cases the flows were well predicted by a model where apical constriction drives hydrodynamic flow of the cytoplasm (Fig. 3g–l, Extended Data Figs 9 and 10 and Supplementary Methods).

To compare cell shape changes in the wild type and acellular embryos directly, we plotted virtual cells onto the flow field and tracked their motion over time (Fig. 4a, b and Supplementary Video 9). Remarkably, virtual cells in the acellular embryos undergo morphological changes similar to those in the wild type as long as the reduced rate of apical constriction is compensated for (Fig. 4b–f and Supplementary Video 9). In particular, in both cases, virtual cell lengthening is achieved by a quasi-linear uniform extension of the apical portion of the cell (0–20  $\mu\text{m}$ ) (Fig. 4g). Thus, the region-specific changes in cell shape that normally occur during lengthening can be produced by laminar flow of the cytoplasm independent of the mechanical inputs from the basolateral membranes (Fig. 4h). On the other hand, the virtual cells in the acellular embryo do not undergo shortening or basal widening, and the furrow

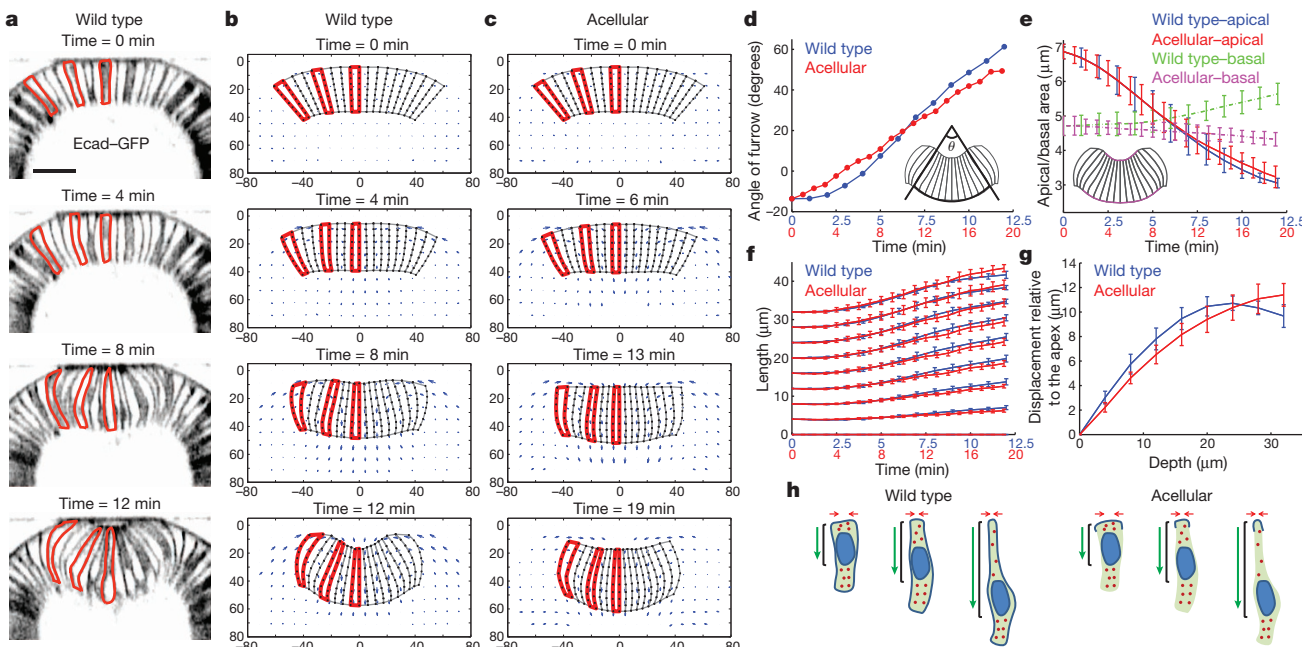


**Figure 4 | Virtual cell analysis to show cell shape changes from the flow.**

a, Ventral furrow formation in the wild-type embryo. Selected cells are highlighted for better comparison. Scale bar, 30  $\mu\text{m}$ . b, c, Virtual cells for the wild-type (b) and acellular (c) embryos. d–f, The secant angle enclosed by the middle 12 ventral cells (d), their average apical and basal area (e) and the

is never fully invaginated (Fig. 4e and Supplementary Videos 7–9), suggesting that some extra, cell-dependent mechanisms are required during the shortening phase.

In summary, we demonstrate that during the lengthening phase of ventral furrow formation, the behaviour of the bulk tissue below the apical cortex closely corresponds to that of a viscous fluid, although it is composed of heterogeneous cellular organelles and is partitioned into individual cells with plasma membrane boundaries. On the basis of preliminary data in our laboratory, the tissue interior is unlikely to be elastic (Extended Data Fig. 4d, Supplementary Video 10 and Supplementary Notes). In line with that, the measured flow profiles closely agree with the hydrodynamic predictions throughout the lengthening phase even after substantial tissue deformation has occurred (Extended Data Fig. 4b, c). The rate of the cytoplasmic flow is always proportional to the rate of apical constriction independent of time (Fig. 3k–m). Consistently, we found that the viscous model fits our data much better than a linear elastostatic one (90% versus 75% agreement; Supplementary Notes).

The importance of the hydrodynamic properties of the cytoplasm has been implicated in processes occurred in continuous cytoplasm, such as cytoplasmic streaming in single large cells of algae<sup>18</sup>, the one-cell stage of *Caenorhabditis elegans* embryos<sup>19</sup> or the *Drosophila* oocyte<sup>20</sup>. Our work demonstrates that even in the context of multicellular tissues, stresses generated at the surface of the tissue can integrate with the hydrodynamic properties of the interior to transmit force and determine the specific changes in cell shape that characterize morphogenesis. This mechanism is surprisingly independent of the plasma membrane between neighbouring cells and may not require specific molecular components. Because apical constriction-induced epithelial folding occurs frequently in development (for example, *Drosophila* tracheal pit invagination<sup>21</sup>, *Xenopus* bottle cell formation<sup>22</sup> and neural tube closure<sup>23</sup>), using viscous flow to transmit force may represent a fundamental mechanism in morphogenesis.

## METHODS SUMMARY

To measure the motion of cytoplasm, we injected 500-nm red fluorescent carboxylated polystyrene microspheres (Invitrogen) into developing embryos at the late

average distance between the cell apex and each lateral node (f) as a function of time. g, The displacement of lateral nodes along the AB axis as a function of their initial AB positions. Error bars, s.d. in e–g. h, Cartoon model demonstrating that in response to apical constriction, the apical cytoplasm undergoes uniform extension independent of the basolateral membrane.

syncytial or cellularization stage using a FemtoJet express microinjector (Eppendorf). To label the plasma membrane, we coated the beads with WGA-Alexa Fluor 488 (Invitrogen) using a Carbodiimide Kit for covalent coupling (Polysciences) and injected them into the perivitelline space of the cellularizing embryos. The WGA beads bind to the plasma membrane immediately after injection and remain bound throughout development.

Injected embryos were subjected to two-photon live imaging with an excitation wavelength of 920 nm. Stacks of 40 images taken at 2- $\mu\text{m}$  steps were recorded every 8 s. The images were 256 pixels  $\times$  128 pixels, corresponding to 150- $\mu\text{m}$  (medial-lateral)  $\times$  75- $\mu\text{m}$  (anterior-posterior) regions approximately centred at the ventral midline. Using MATLAB (MathWorks) we developed methods to determine the three-dimensional trajectory of beads and to generate the velocity field of cytoplasmic flow in the course of ventral furrow formation. Each velocity field (80  $\times$  40 grid of 2- $\mu\text{m}$  squares projected on the plane of transverse cross section) was calculated by averaging bead measurements over a 2-min time span with a sampling radius of 18  $\mu\text{m}$ .

The measurements and the prediction of the Stokes equations were compared as follows. We considered a sub-domain of the embryo cross section where velocity distribution could be estimated with sufficient accuracy. The boundary of this domain was specified by a discrete curve (polygon) discretized by 200 equally spaced boundary points. Stokes flow in the interior of this polygon was constructed as superposition of two-dimensional Stokeslets centred at those boundary points. The procedure allowed a parameter-free comparison between the measurements and hydrodynamic predictions.

Detailed information about reagents and methods used in this paper is described in Methods and Supplementary Methods.

**Online Content** Any additional Methods, Extended Data display items and Source Data are available in the online version of the paper; references unique to these sections appear only in the online paper.

Received 27 July 2013; accepted 20 January 2014.

Published online 2 March 2014.

1. Sawyer, J. M. et al. Apical constriction: a cell shape change that can drive morphogenesis. *Dev. Biol.* **341**, 5–19 (2010).
2. Leptin, M. & Grunewald, B. Cell shape changes during gastrulation in *Drosophila*. *Development* **110**, 73–84 (1990).
3. Sweeton, D., Parks, S., Costa, M. & Wieschaus, E. Gastrulation in *Drosophila*: the formation of the ventral furrow and posterior midgut invaginations. *Development* **112**, 775–789 (1991).
4. Martin, A. C., Kaschube, M. & Wieschaus, E. F. Pulsed contractions of an actin-myosin network drive apical constriction. *Nature* **457**, 495–499 (2009).

5. Odell, G. M., Oster, G., Alberch, P. & Burnside, B. The mechanical basis of morphogenesis. I. Epithelial folding and invagination. *Dev. Biol.* **85**, 446–462 (1981).
6. Brodland, G. W., Viens, D. & Veldhuis, J. H. A new cell-based FE model for the mechanics of embryonic epithelia. *Comput. Methods Biomed. Eng.* **10**, 121–128 (2007).
7. Conte, V., Munoz, J. J., Baum, B. & Miodownik, M. Robust mechanisms of ventral furrow invagination require the combination of cellular shape changes. *Phys. Biol.* **6**, 016010 (2009).
8. Brodland, G. W. & Clausi, D. A. Embryonic tissue morphogenesis modeled by FEM. *J. Biomech. Eng.* **116**, 146–155 (1994).
9. Pouille, P. A. & Farge, E. Hydrodynamic simulation of multicellular embryo invagination. *Phys. Biol.* **5**, 015005 (2008).
10. Conte, V. et al. A biomechanical analysis of ventral furrow formation in the *Drosophila melanogaster* embryo. *PLoS ONE* **7**, e34473 (2012).
11. Kaplan, D. R. & Hagemann, W. The relationship of cell and organism in vascular plants. *Bioscience* **41**, 693–703 (1991).
12. Davidson, L. A. Embryo mechanics: balancing force production with elastic resistance during morphogenesis. *Curr. Top. Dev. Biol.* **95**, 215–241 (2011).
13. Mason, T. G., Ganeshan, K., van Zanten, J. H., Wirtz, D. & Kuo, S. C. Particle tracking microrheology of complex fluids. *Phys. Rev. Lett.* **79**, 3282–3285 (1997).
14. Wirtz, D. Particle-tracking microrheology of living cells: principles and applications. *Annu. Rev. Biophys.* **38**, 301–326 (2009).
15. Lecuit, T. & Wieschaus, E. Polarized insertion of new membrane from a cytoplasmic reservoir during cleavage of the *Drosophila* embryo. *J. Cell Biol.* **150**, 849–860 (2000).
16. Lecuit, T., Samanta, R. & Wieschaus, E. *slam* encodes a developmental regulator of polarized membrane growth during cleavage of the *Drosophila* embryo. *Dev. Cell* **2**, 425–436 (2002).
17. Leptin, M. *twist* and *snail* as positive and negative regulators during *Drosophila* mesoderm development. *Genes Dev.* **5**, 1568–1576 (1991).
18. Goldstein, R. E., Tuval, I. & van de Meent, J. W. Microfluidics of cytoplasmic streaming and its implications for intracellular transport. *Proc. Natl Acad. Sci. USA* **105**, 3663–3667 (2008).
19. Niwayama, R., Shinohara, K. & Kimura, A. Hydrodynamic property of the cytoplasm is sufficient to mediate cytoplasmic streaming in the *Caenorhabditis elegans* embryo. *Proc. Natl Acad. Sci. USA* **108**, 11900–11905 (2011).
20. Glotzer, J. B., Saffrich, R., Glotzer, M. & Ephrussi, A. Cytoplasmic flows localize injected *oskar* RNA in *Drosophila* oocytes. *Curr. Biol.* **7**, 326–337 (1997).
21. Brodu, V. & Casanova, J. The RhoGAP *crossveinless-c* links *tracheless* and EGFR signaling to cell shape remodeling in *Drosophila* tracheal invagination. *Genes Dev.* **20**, 1817–1828 (2006).
22. Hardin, J. & Keller, R. The behaviour and function of bottle cells during gastrulation of *Xenopus laevis*. *Development* **103**, 211–230 (1988).
23. Sadler, T. W. Embryology of neural tube development. *Am. J. Med. Genet. C. Semin. Med. Genet.* **135C**, 2–8 (2005).

**Supplementary Information** is available in the online version of the paper.

**Acknowledgements** We thank S. Thibierge (Imaging core facility) for two-photon microscopy. We thank N. Wingreen, C. Brangwynne, C. Brody, H. Stone, S. Little, S. Di Talia, Y.-C. Wang and Y. Yan for their suggestions on the manuscript. We thank all members of the Wieschaus and Schupbach laboratories for discussions. This work was supported by the National Institutes of Health (National Institute of Child Health and Human Development grant 5R37HD15587) to E.F.W. and by the Howard Hughes Medical Institute. B.H. was supported by the New Jersey Commission on Cancer Research Fellowship. The Imaging core facility was supported by National Institutes of Health Grant P50 GM 071508.

**Author Contributions** B.H., K.D., O.P. and E.W. designed the study, performed the experiments and analysed the data. B.H. wrote the first draft of the manuscript. All authors participated in discussion of the data and in producing the final version of the manuscript.

**Author Information** Reprints and permissions information is available at [www.nature.com/reprints](http://www.nature.com/reprints). The authors declare no competing financial interests. Readers are welcome to comment on the online version of the paper. Correspondence and requests for materials should be addressed to E.W. ([efw@princeton.edu](mailto:efw@princeton.edu)).

## METHODS

**Fly stocks and genetics.** The following fluorescent fusion protein stocks were used: myosin–green fluorescent protein (GFP) (*sqh-GFP*)<sup>24</sup>, E-cadherin–GFP (*ubi-DEcad-GFP*)<sup>25</sup> and H2Av–GFP<sup>26</sup>. Acellular embryos were generated using a *Df(2L)dpp[s7-dp35]21F1-3;22F1-2(halo)* *Df(2L)Exel6016(slam)P(SUPor-P)CG42748<sup>KG09309</sup>* (*CG34137*)/*Cyo sqh-GFP* line. The *P(SUPor-P)CG42748<sup>KG09309</sup>* line<sup>27</sup> and the *UAS-shRNA-zip* line were obtained from Bloomington *Drosophila* Stock Center. The mutant chromosome was marked with *Df(2L)dpp[s7-dp35]21F1-3;22F1-2(halo)* to allow homozygous embryos to be distinguished from their heterozygous siblings soon after the beginning of cell cycle 14 on the basis of the continued presence of lipid droplets within the periplasm (the ‘halo’ phenotype<sup>28</sup>). The homozygous mutant embryos faithfully reproduced the acellular phenotype of the 2L–embryos<sup>29</sup> with complete penetrance. *sqh-GFP* was recombined with *cta/Cyo; T48* (ref. 30) to generate *cta/Cyo; T48 sqh-GFP*. Because Cta is maternally supplied<sup>31</sup>, *cta; T48 sqh-GFP* flies were selected from the balanced stock to produce *cta; T48* double-mutant embryos. *cta/Cyo; T48 sqh-GFP* flies from the same stock were selected to produce *T48 sqh-GFP* embryos with maternally supplied Cta. *cta; sqh-GFP/ T48 sqh-GFP* females were crossed to *cta/Cyo; sqh-GFP* males to produce *cta/(cta or Cyo); sqh-GFP/(sqh-GFP or T48 sqh-GFP)* embryos which lack maternally supplied Cta but have at least one copy of wild-type *T48* (*cta* mutant embryos). To generate embryos with *zip* knockdown, *UAS-shRNA-zip* females were crossed to *Maternal-Tubulin-Gal4; spider-GFP* males to generate *UAS-shRNA-zip/ Maternal-Tubulin-Gal4; spider-GFP/+* females. Embryos derived from such females were used as *zip* knockdown mutants (*zip-RNAi*).

**Injection of fluorescent beads into *Drosophila* embryos.** To inject inert fluorescent beads into the cytoplasm of the embryos, manually staged embryos were collected at 25 °C on agar plates, dechorionated in 50% bleach for 2–4 min, rinsed thoroughly with water and transferred on a coverslip covered with a thin layer of glue. The embryos were subject to moderate dehydration in a desiccator for 10–15 min, and then covered with halocarbon oil (Sigma, S700:S27 = 3:1) in which they continued to develop normally. Adapting a general microinjection protocol developed for *Drosophila* transformation, a suspension of 500-nm red fluorescent carboxylated polystyrene microspheres (Invitrogen, 1:200 final dilution in water) was injected into developing embryos at the late syncytial or cellularization stage using the FemtoJet express microinjector (Eppendorf). Injection was performed at approximately 50% egg length at 18 °C. Injected embryos were subjected to live imaging by confocal or two-photon microscopy at room temperature (~22 °C). The injected beads usually remain suspended in the cytoplasm without forming aggregates, and do not seem to adhere to the plasma membrane or nuclei. When injected before or during early cellularization stages, beads deposited in the cytoplasm become enclosed within the newly formed cells by the end of cellularization. During cellularization when there is no global movement of the tissue, the beads show extremely low mobility (Extended Data Fig. 2 and Supplementary Methods), consistent with a high effective viscosity of the cytoplasm<sup>34</sup>. The injection procedure has no obvious effect on the development of the embryos, as they gastrulate normally and eventually hatch.

To prepare WGA-coated beads for injection, 500 nm red fluorescent carboxylated microspheres (Invitrogen) were coated with WGA-Alexa Fluor 488 (Invitrogen) using a Carbodiimide Kit for covalent coupling (Polysciences). Before use, the WGA beads were briefly sonicated and filtered through an Ultrafree-MC centrifugal filter device (Millipore, pore size 0.65 μm) to remove large clumps. To label the plasma membrane, the filtered beads were injected into the perivitelline space of the cellularizing embryos and followed by two-photon microscopy at room temperature. The WGA beads bind to the plasma membrane immediately after injection and remain bound throughout development. When injected at different stages of cellularization, the WGA beads bind to different regions of the plasma membrane, providing trackable markers along the entire lateral membrane (Fig. 2a, Extended Data Fig. 5a and Supplementary Videos 2 and 3). Beads injected at very early cellularization localize to the furrow canals (the front of the growing membrane furrow) throughout cellularization. When injected during mid-cellularization, the beads bind the incipient lateral membrane and move in register with the advancing furrow canals. Finally, beads injected during late cellularization remain in the apical region of the cell and do not follow the rapid movement of the invaginating membrane. During cellularization, while the cytoplasmic beads predominantly undergo random motion, the WGA beads show directional, basal movement that corresponds well to the previously described pattern of membrane growth<sup>15</sup> (Extended Data Fig. 5b–d).

**Live imaging.** To measure the movement of cytoplasm during ventral furrow formation, embryos injected with the cytoplasmic beads were subjected to two-photon live imaging with a custom-built two-photon scanning microscope<sup>32</sup> built around an upright Olympus BX51. Fluorescence emissions were collected both through an objective (numerical aperture 0.8 Olympus water immersion objective ×40 LUMPlanFl/IR, or numerical aperture 0.8 oil immersion objective ×25) and

through a numerical aperture 1.3 oil condenser lens and detected with high quantum efficiency hand-peaked GaAsP photomultipliers (Hamamatsu). The microscope was operated by the MATLAB software ScanImage<sup>33</sup> modified to control a piezo objective (PI) and to allow laser power to be increased with greater imaging depth. Images were taken with an excitation wavelength of 920 nm. Stacks of 40 images taken at 2-μm steps were recorded every 8 s. The temporal resolution was chosen to be sufficiently high to resolve the movement of individual beads. The images are 256 pixels × 128 pixels, corresponding to 150-μm (medial-lateral) × 75-μm (anterior-posterior) regions approximately centred at the ventral midline. The signal sampling time per pixel was 3.2 μs. Cell membrane (E-cadherin–GFP) or myosin II (Sqh–GFP) was imaged simultaneously to monitor the progress of cellularization and gastrulation.

To measure the apparent diffusion coefficient of beads within the cytoplasm, cellularizing embryos injected with inert beads were imaged with a Leica SP5 single-photon confocal microscope, a 63×/1.3 numerical aperture glycerine immersion objective, an argon ion laser and a 561-nm diode laser. Images were acquired using a pinhole setting from 1 to 2 Airy units and an excitation band-pass to 495–575 nm to detect GFP and 575–655 nm to detect red fluorescent beads. Stacks of 16–20 images taken at 2-μm steps were recorded every 1–2 s. The images are 128 pixels × 128 pixels, corresponding to 40-μm (medial-lateral) × 40-μm (anterior-posterior) regions approximately centred at the ventral midline.

**Particle tracking and estimation of the measurement error.** The three-dimensional image stacks recording the motion of the beads were pre-processed at every time point with a band-pass filter with a lower bound of one voxel and an upper bound of about eight voxels. The position of the beads was initially determined to voxel accuracy by finding the highest intensity centroid voxel for each bead intensity distribution and then subsequently fine-tuned to sub-voxel accuracy by fitting a three-dimensional Gaussian shape to this centroid voxel. To estimate the accuracy of the measurement of the bead position, we measured the apparent displacement of immobilized beads on a glass cover slip. We found that the typical resolution for the immobilized beads was 0.023 μm in the lateral direction and 0.09 μm in the axial direction. In the embryo, the accuracy of the determination of the bead positions was found to be  $\delta x \approx \pm 0.11 \mu\text{m}$  in the lateral direction and  $\delta z \approx \pm 0.50 \mu\text{m}$  in the axial direction<sup>34</sup>. The roughly fourfold decrease in the spatial resolution is probably due to the increased background noise present in the embryo.

Once the positions of the beads had been determined, we applied a tracking algorithm to connect the beads over time and determine their trajectories. We considered two consecutive frames corresponding to times *t* and *t* + 1 and define  $r_{ij}(t)$  to be the displacement vector between *i*th bead in frame *t* and *j*th bead in frame *t* + 1. We next determined the pair of beads that corresponded to the smallest distance from the set of all displacement vectors. In this way we established a one-to-one correspondence between two beads of two consecutive frames. By removing these first two beads from their respective time frames and reiterating, we established a correspondence between another bead pair. Once either the set of beads at time *t* or *t* + 1 had been exhausted, we arrived at a set of one-to-one connections that allowed us to track bead motion through the two consecutive time frames. To judge whether a pair of beads could be tracked into the next (*t* + 2) frame, we determined whether consecutive iterations gave the same groupings/trajectories as a protocol in which the middle frame had been skipped. If the two protocols did not generate the same trajectory between frames *t* and *t* + 2, then the trajectory corresponding to bead *i* was terminated at time frame *t*.

### Theoretical analysis of the motion of viscous fluids at low Reynolds numbers.

1. Legitimizing the use of the linear Stokes equations. Given the typical length scale of the ventral furrow invagination ( $L = 100 \mu\text{m}$ ) and the velocity of the flow ( $V < 5 \mu\text{m min}^{-1}$ ), and if we assume that the cytoplasm has a viscosity as low as that of water ( $\rho = 10^3 \text{ kg m}^{-3}$ ,  $\eta = 0.89 \text{ cP}$ ), the cytoplasmic flow driven by apical constriction is thus characterized by a Reynolds number of

$$\text{Re} = \frac{\rho VL}{\eta} = 10^{-5}$$

Because the cytoplasm of the living cells has a viscosity necessarily higher than water, this validates the use of the linear Stokes equations.

2. Comparison between the measurements and the prediction of the Stokes equations. Comparison between the experimentally determined tissue deformation and the dynamics specified by the Stokes equations was performed as follows. We considered a sub-domain of the embryo cross section where velocity distribution could be estimated with sufficient accuracy. The boundary of this (arbitrary) domain was specified by a discrete curve (polygon) discretized by 200 equally spaced boundary points. Stokes flow in the interior of this polygon was constructed as superposition of two-dimensional Stokeslets centred at those boundary points. Explicitly, velocity  $v(r)$  at position *r* is given by<sup>35,36</sup>

$$\nu(r) = \frac{1}{4\pi\mu} \sum_{k=1}^{200} S(\hat{r})f(r_k)$$

where  $\mu$  is dynamic viscosity,  $f(r_k)$  is the (yet to be determined) force monopole at the  $k$ th boundary node and  $S$  is the two-dimensional Oseen tensor given by

$$S_{ij}(\hat{r}) = \delta_{ij} \log(r) - \frac{\hat{r}_i \hat{r}_j}{r^2}$$

with  $\hat{r} = r - r_k$  and  $r = |\hat{r}|$ .

It may be verified that the above expression solves the Stokes equations

$$-\nabla p + \mu \nabla^2 \nu = 0$$

$$\nabla \cdot \nu = 0$$

for any choice of force monopoles  $f(r_k)$ . Finally, the force monopoles  $f(r_k)$  were chosen to best match velocities in a narrow rim of points in the vicinity of the boundary. In general, this optimization problem is very ill-posed because very dissimilar boundary force distributions may give rise to similar flows. This is, however, inconsequential for the present analysis because we seek to reconstruct the flow distribution rather than boundary stresses that drive those flows. In practice, we adopted the following regularization scheme for our analysis. The above discretized equations lead to a linear system of the form  $Ax = b$ . To regularize singular matrix  $A$ , we added to it a small multiple of unity matrix  $\varepsilon I$ . We checked that the choice of  $\varepsilon$  does not significantly influence the result of regularization procedure.

The procedure outlined above gives a parameter-free fit and thus does not allow overfitting. Specifically, velocity distribution in the interior of the domain is uniquely determined by velocity distribution at its boundary. In particular, the knowledge of cytoplasmic viscosity is not required for performing the comparison.

The relative difference (RD) between the measured velocity fields and the theoretical predictions was given by:

$$RD = \frac{V_{\text{data}} - V_{\text{theory}}}{(\overline{V}_{\text{data}} + \overline{V}_{\text{theory}})/2}$$

where  $V_{\text{data}}$  and  $V_{\text{theory}}$  are the measured and predicted velocity field, respectively, and  $\overline{V}_{\text{data}}$  and  $\overline{V}_{\text{theory}}$  are the average velocity of the velocity field. An average relative difference (RD) was calculated for each time point.

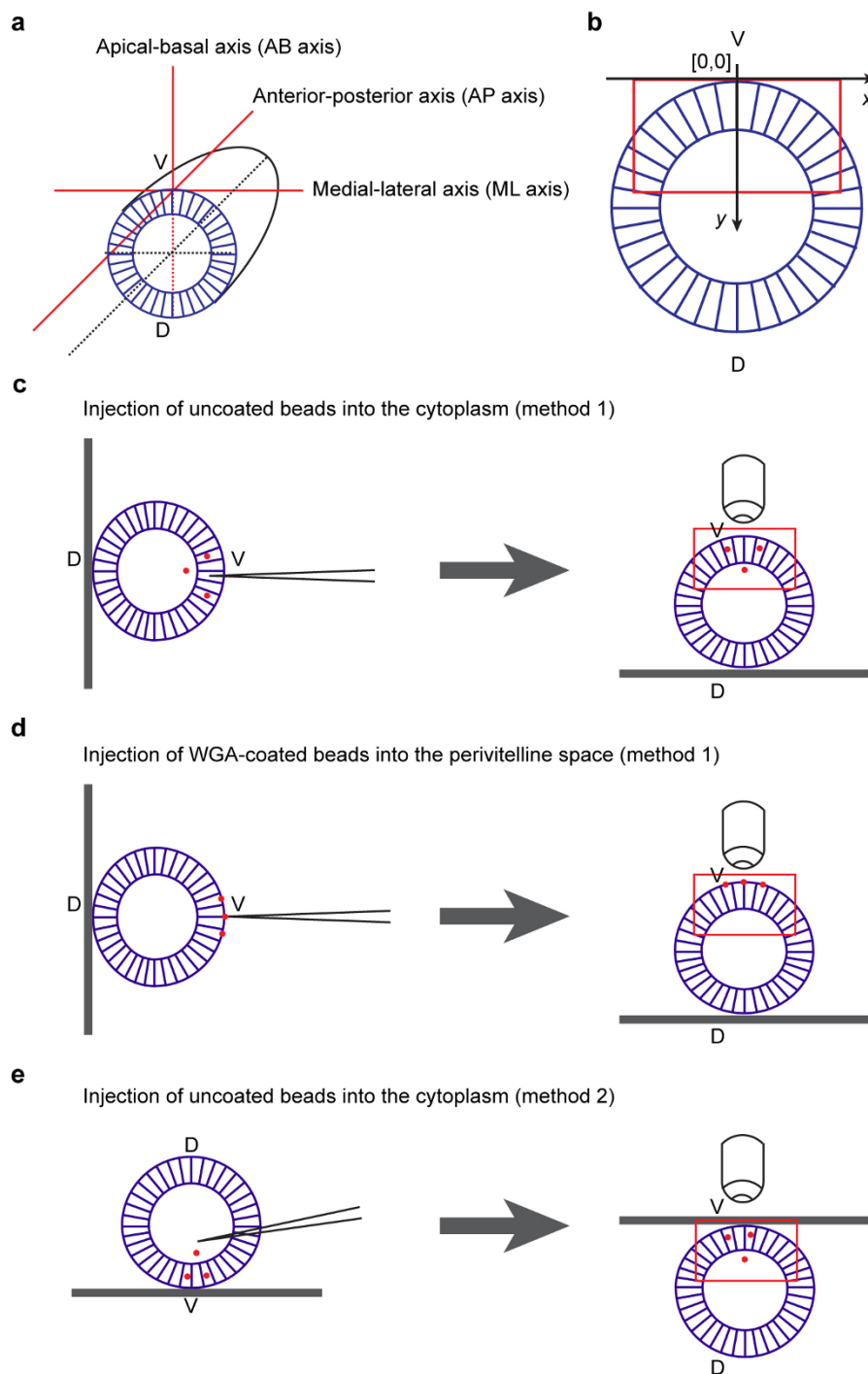
The source code for particle tracking and theoretical analysis used in this paper is available upon request.

**Antibody staining.** Antibody staining against myosin (Zipper), Neurotactin (Neur), Armadillo (Arm), Twist and Snail were performed on heat-fixed or formaldehyde-fixed embryos, as described in ref. 37. The vitelline membrane was removed by shaking in heptanes and methanol after fixation. Embryos were blocked with 10% BSA in PBS and 0.1% Tween 20, and incubated with primary antibodies in PBT

(PBS/0.1% BSA/0.1% Tween 20) overnight at 4 °C with the following dilutions: rabbit anti-Zipper 1:100; monoclonal mouse anti-Neur (BP106) 1:10 (Hybridoma Bank); monoclonal mouse anti-Arm 1:50 (Hybridoma Bank); polyclonal rat anti-Twist or anti-Snail 1:500. Secondary antibodies coupled to Alexa Fluor 488, Alexa Fluor 561 and Alexa Fluor 647 were used at 1:500 (Invitrogen). Embryos were mounted in Aqua Poly Mount (Polysciences) for confocal imaging.

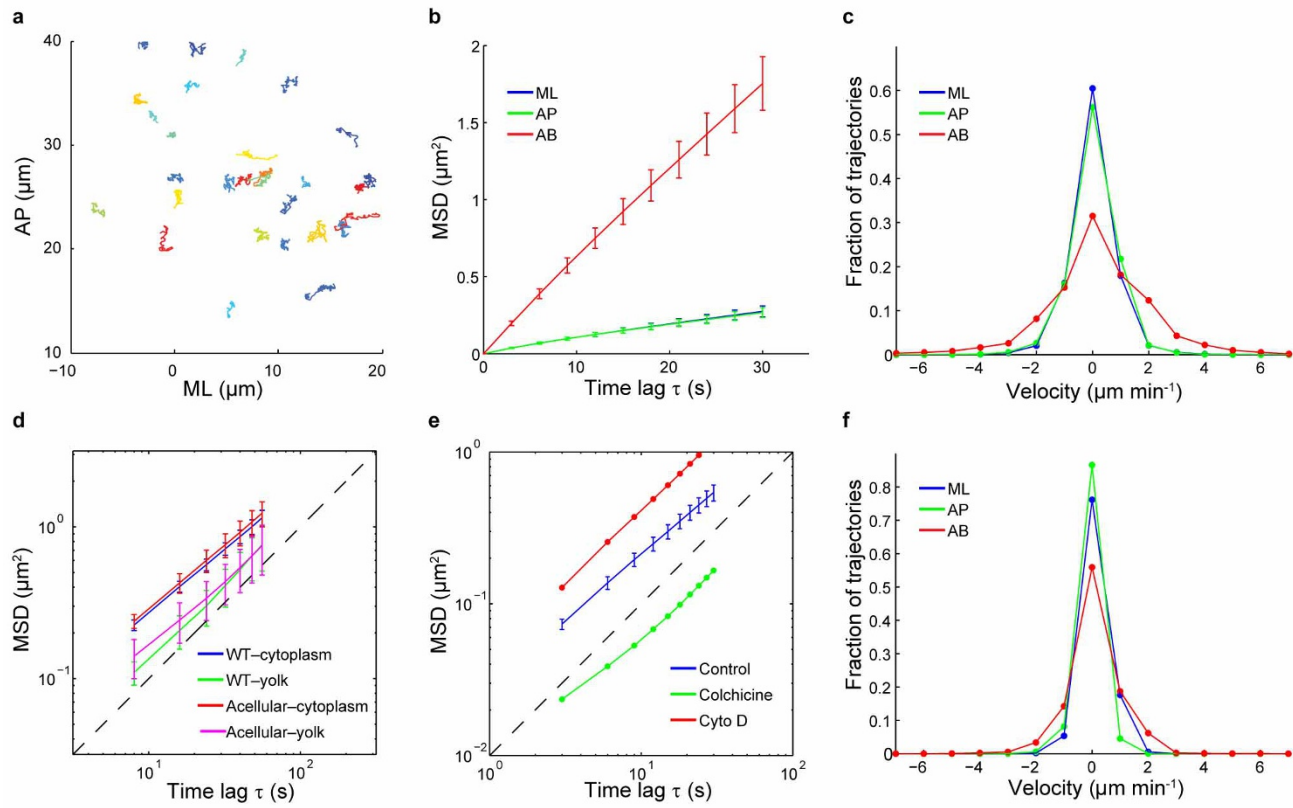
**Scanning electron microscopy.** Embryos were collected at desired stages, dechorionated, fixed with 2.5% glutaraldehyde in heptane and hand peeled in PBS. Embryos were then post-fixed in 1% osmium tetroxide and dehydrated through an ethanol series. They were dried using HDMS (Electron Microscopy Sciences), coated with gold palladium in a Denton Desk II sputter coater, and examined and photographed in a JEOL 840 scanning electron microscope.

24. Royou, A., Sullivan, W. & Karess, R. Cortical recruitment of nonmuscle myosin II in early syncytial *Drosophila* embryos: its role in nuclear axial expansion and its regulation by Cdc2 activity. *J. Cell Biol.* **158**, 127–137 (2002).
25. Oda, H. & Tsukita, S. Real-time imaging of cell-cell adherens junctions reveals that *Drosophila* mesoderm invagination begins with two phases of apical constriction of cells. *J. Cell Sci.* **114**, 493–501 (2001).
26. Clarkson, M. & Saint, R. A. His2AvDGFP fusion gene complements a lethal His2AvD mutant allele and provides an in vivo marker for *Drosophila* chromosome behavior. *DNA Cell Biol.* **18**, 457–462 (1999).
27. Bellen, H. J. et al. The BDGP gene disruption project: single transposon insertions associated with 40% of *Drosophila* genes. *Genetics* **167**, 761–781 (2004).
28. Welte, M. A., Gross, S. P., Postner, M., Block, S. M. & Wieschaus, E. F. Developmental regulation of vesicle transport in *Drosophila* embryos: forces and kinetics. *Cell* **92**, 547–557 (1998).
29. Merrill, P. T., Sweeton, D. & Wieschaus, E. Requirements for autosomal gene activity during precellular stages of *Drosophila melanogaster*. *Development* **104**, 495–509 (1988).
30. Kolsch, V., Seher, T., Fernandez-Ballester, G. J., Serrano, L. & Leptin, M. Control of *Drosophila* gastrulation by apical localization of adherens junctions and RhoGEF2. *Science* **315**, 384–386 (2007).
31. Parks, S. & Wieschaus, E. The *Drosophila* gastrulation gene concertina encodes a G alpha-like protein. *Cell* **64**, 447–458 (1991).
32. Denk, W., Strickler, J. H. & Webb, W. W. Two-photon laser scanning fluorescence microscopy. *Science* **248**, 73–76 (1990).
33. Pologruto, T. A., Sabatini, B. L. & Svoboda, K. ScanImage: flexible software for operating laser scanning microscopes. *Biomed. Eng. Online* **2**, 13 (2003).
34. Savin, T. & Doyle, P. S. Static and dynamic errors in particle tracking microrheology. *Biophys. J.* **88**, 623–638 (2005).
35. Happel, J. R. & Brenner, H. *Low Reynolds Number Hydrodynamics: With Special Applications to Particulate Media* (Prentice-Hall, 1965).
36. Pozrikidis, C. Interfacial dynamics for Stokes flow. *J. Comput. Phys.* **169**, 250–301 (2001).
37. Peifer, M., Sweeton, D., Casey, M. & Wieschaus, E. wingless signal and Zeste-white 3 kinase trigger opposing changes in the intracellular distribution of Armadillo. *Development* **120**, 369–380 (1994).



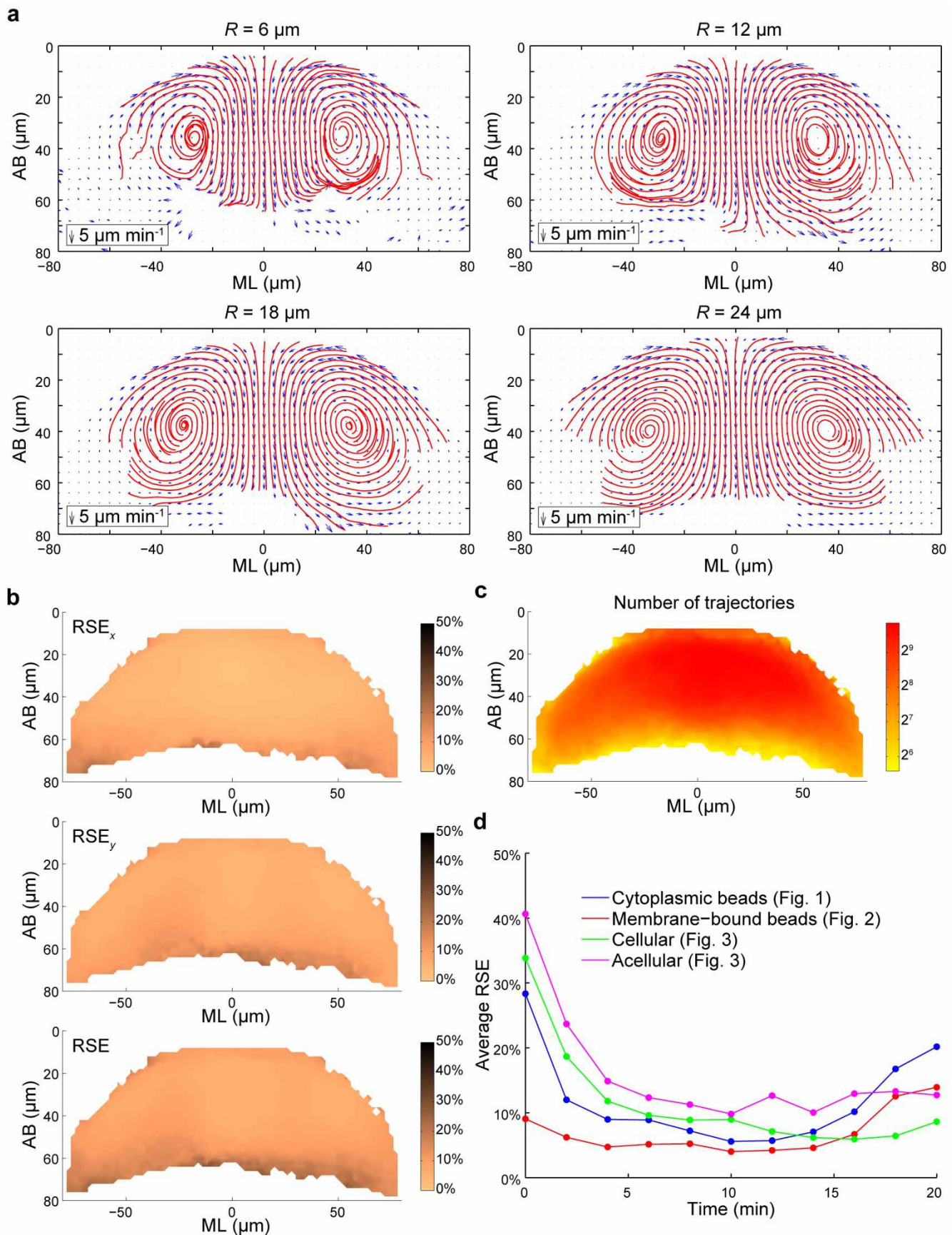
**Extended Data Figure 1 | Embryo orientation for bead injection and live imaging.** **a**, Body axis (red lines) of the *Drosophila* embryo. A transverse cross section of the embryo at 50% egg length is shown in blue. V, ventral; D, dorsal. **b**, The definition of  $x$ ,  $y$  coordinates used in this study.  $x$  axis, ML axis;  $y$  axis, AB axis. **c**, **d**, Injection of uncoated fluorescent beads (**c**) or WGA-coated beads (**d**) into the cytoplasm or the perivitelline space of an embryo, respectively. The embryo is glued to the coverslip on its dorsal side (method 1). **e**, Injection of uncoated fluorescent beads into the cytoplasm of an embryo with

its ventral side glued to a coverslip (method 2). Method 1 is better suited than method 2 for introducing beads into the perivitelline space, whereas method 2 has the advantage of keeping the ventral side free of wound. Note that in method 2 the ventral surface of the embryo is slightly flattened owing to contact with the coverslip. This nevertheless does not affect the hydrodynamic characteristics of the cytoplasmic flow. Method 1 was applied in experiments used for Figs 1 and 2. Method 2 was applied in experiments used for Figs 3 and 4 and Extended Data Fig. 10.



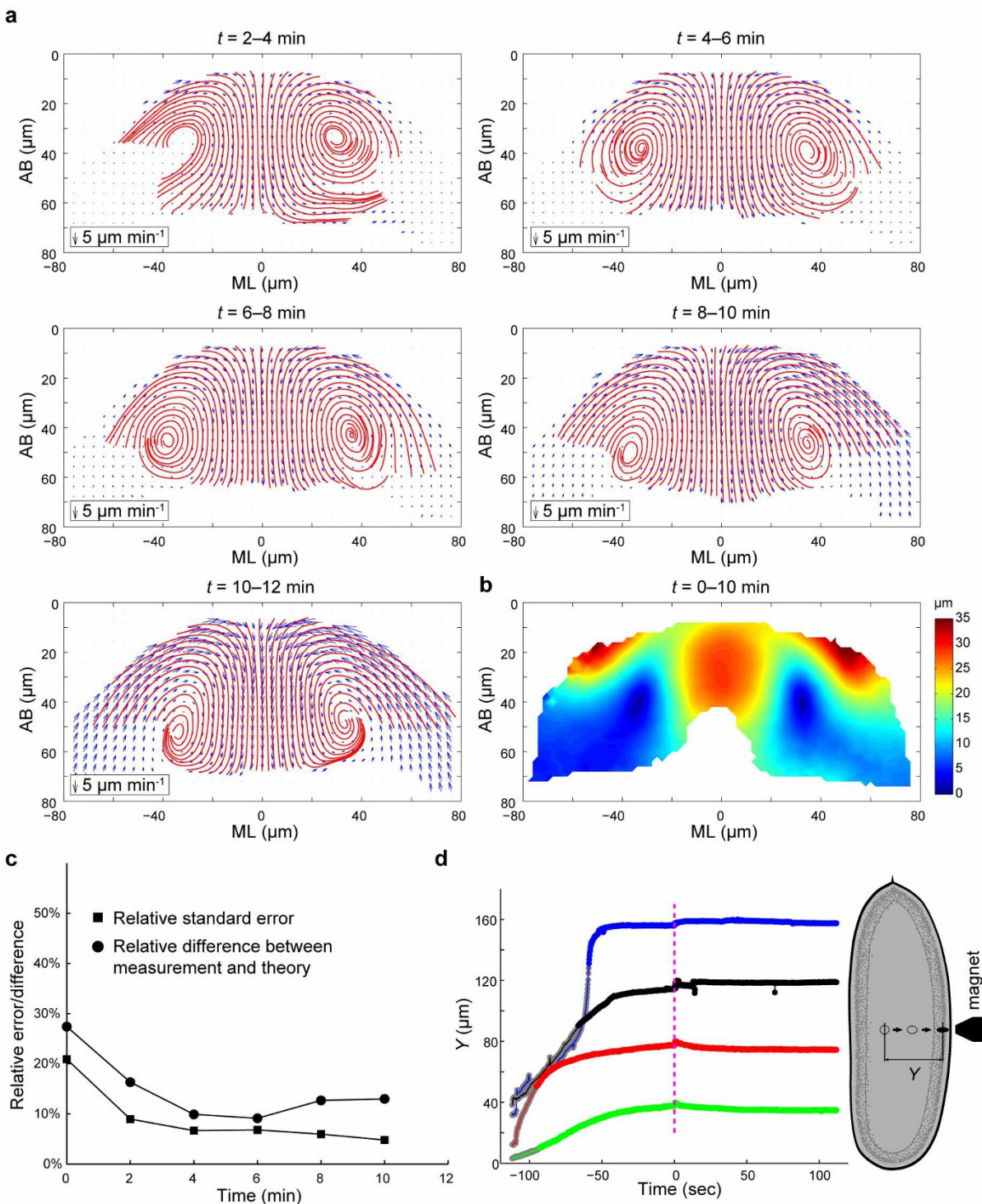
**Extended Data Figure 2 | The cytoplasmic beads show extremely low mobility during cellularization.** **a**, Trajectories of beads in a 2-min interval during cellularization. The projection on the AP–ML plane is shown. Colours are used to distinguish individual trajectories. **b**, Ensemble time-averaged mean squared displacement (MSD) of cytoplasmic beads along the AP, ML and AB axes in cellularizing embryos ( $n = 5$ ). Error bars, s.d. **c**, Distribution of beads velocity along the AP, ML and AB axes. Velocity was calculated over a 1-min time interval. **d**, Log–log plot of the average two-dimensional mean squared displacement of beads (AP–ML plane) embedded in the cytoplasm or

the yolk of the wild-type embryos ( $n = 5$ ) undergoing cellularization, or in the acellular embryos ( $n = 5$ ) at the corresponding stage. Error bars, s.d. **e**, Log–log plot of the average two-dimensional mean squared displacement of beads embedded in the cytoplasm of the control embryos ( $n = 5$ ) or embryos injected with colchicine ( $n = 2$ ) or cytochalasin D ( $n = 2$ ). Error bars, s.d. **f**, Distribution of beads velocity in embryos co-injected with colchicine. Depolymerization of microtubules by colchicine reduces the active, non-equilibrium fluctuations within the cytoplasm and causes a substantial reduction of the beads' mobility, in particular along the AB axis.



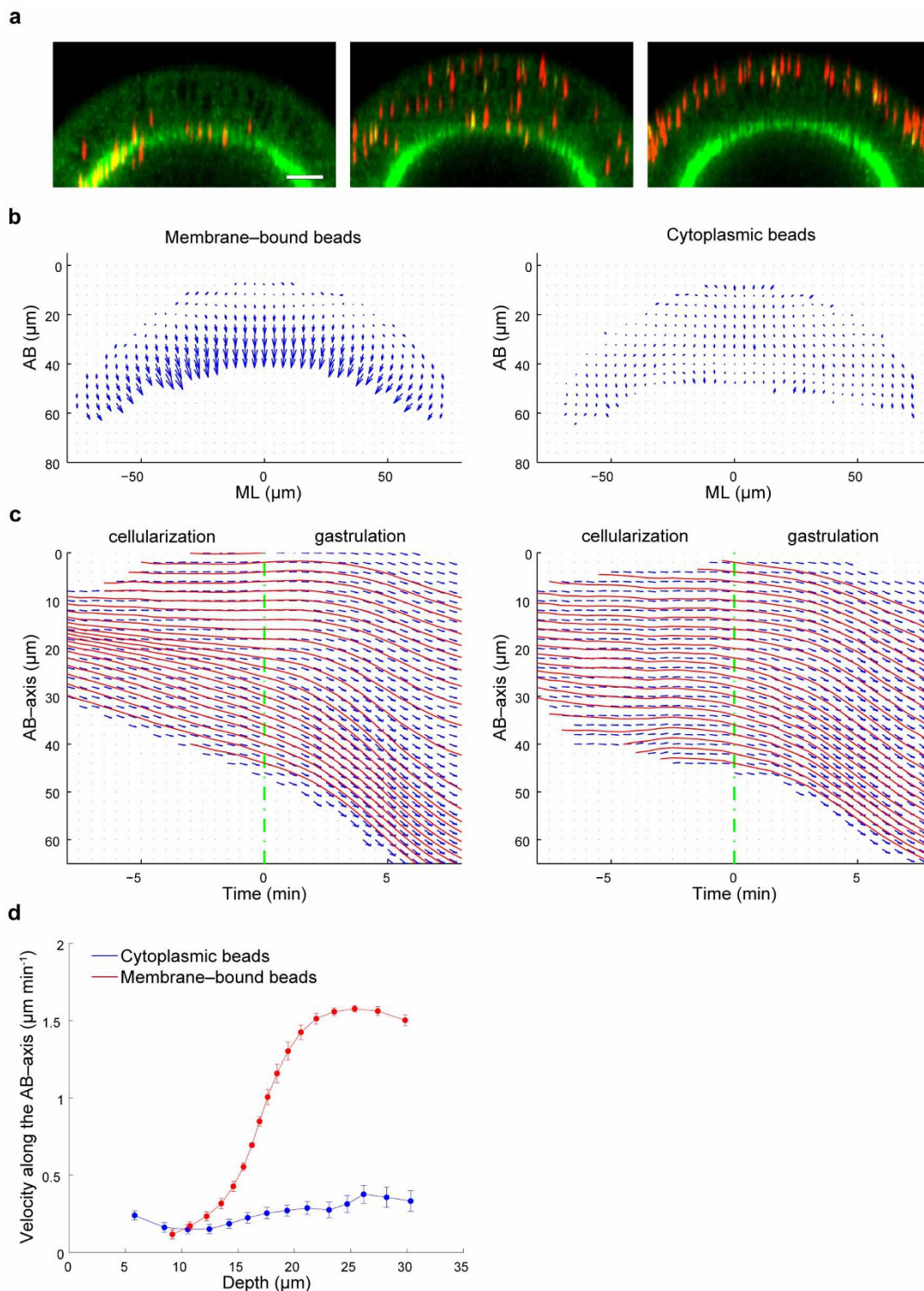
**Extended Data Figure 3 | Generating velocity field and estimating measurement error.** **a**, Velocity fields (blue) and streamlines (red) of the cytoplasmic flow in the wild-type embryos at  $t = 4\text{--}6$  min. Velocity fields were

averaged with different sampling radius  $R$ . We selected an  $R$  value of  $18 \mu\text{m}$  in our study (Supplementary Methods). **b**, Heat maps showing the relative standard error (RSE) for  $V_x$ ,  $V_y$ , and  $V$  ( $\text{RSE}_x$ ,  $\text{RSE}_y$ , and  $\text{RSE}$ , respectively).



**Extended Data Figure 4 | Cytoplasmic flow in the wild-type embryos at different  $t$ .** **a**, Velocity field (blue arrows) and streamlines (red) of the cytoplasmic flow in the wild-type embryos at different time points during ventral furrow formation. The shortening phase starts approximately at  $t = 10–12$  min. **b**, Heat map showing the displacement field between  $t = 0–10$  min. **c**, Relative difference between the measured velocity profiles in the wild-type embryos and the hydrodynamic predictions. Relative standard errors (RSEs) of the velocity profiles are plotted for comparison. Note that the relative difference between measurements and predictions is within 13% between  $t = 4–12$  min. **d**, Displacement of ferrofluid droplets passed through yolk and cytoplasm of syncytial embryos (denoted by  $Y$  in the schematic to the right) plotted against time. Blue curve corresponds to a cellularizing wild-type embryo; other curves are measurements in double-mutant acellular embryos. Magenta dashed line indicates the time point when magnetic field was

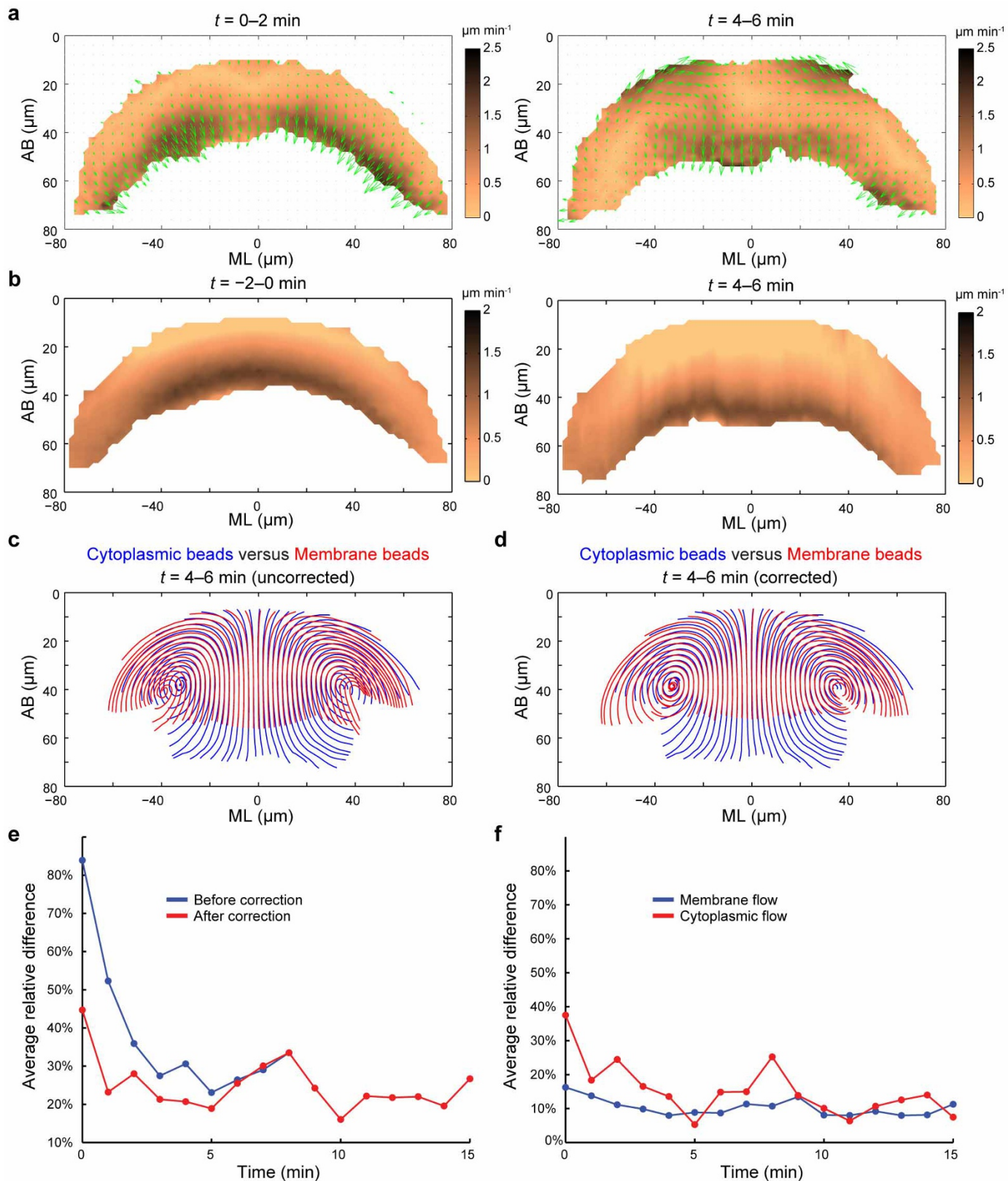
removed ( $t = 0$ ).  $Y$  values are normalized such that 40, 80, 120 and 160  $\mu\text{m}$  correspond to the surface of the embryo for green, red, black and blue curves, respectively. Grey portion of each curve approximately corresponds to the motion of the droplet through the yolk whereas the remainder of the curve corresponds to movement through the cytoplasm layer. Fluctuations in the tracked bead position around  $t = 0$  are due to unsteady motion of the microscope stage as the magnet position was adjusted manually. If these fluctuations are disregarded, droplet behaviour after removal of the magnet is essentially flat. In two of the four cases (the red and green traces), the directionality of the fluctuation is similar to that expected of recoil, but even if interpreted as such, the magnitude does not exceed 5  $\mu\text{m}$ , which is much smaller than the 30- $\mu\text{m}$  displacement of the droplet through the cytoplasmic layer.



**Extended Data Figure 5 | The membrane-bound beads and the cytoplasmic beads show distinct patterns of movement during cellularization.**

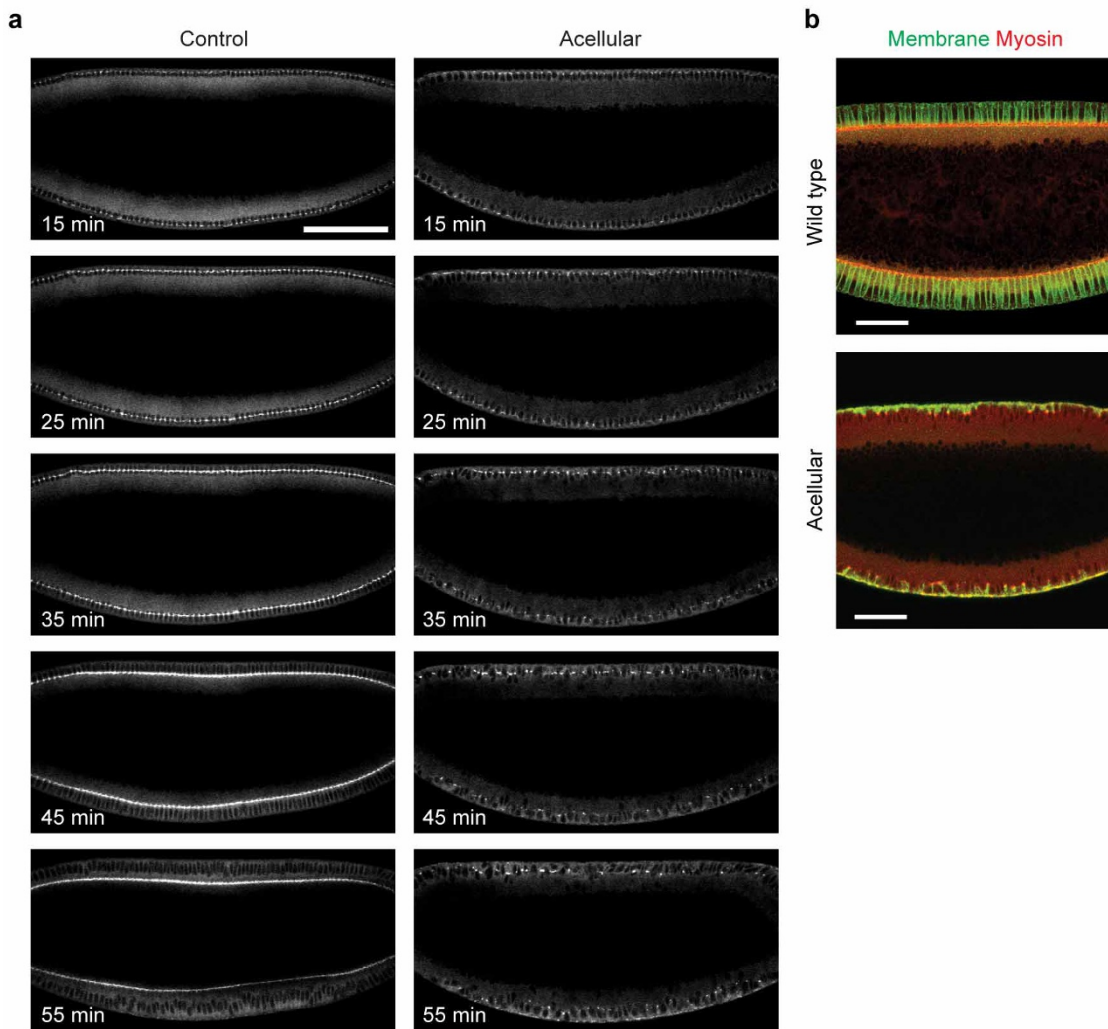
a, Perivitelline injection of WGA-beads at different stages of cellularization leads to their binding to different portions of the plasma membrane. Left: beads injected at very early cellularization are localized to the furrow canals and remain there throughout cellularization. Middle: beads injected during mid-cellularization bind the incipient lateral membrane and move in register with the advancing furrow canals. Right: beads injected during late cellularization remain in the apical region of the cell and do not follow the movement of the furrow canals. Scale bars, 20  $\mu\text{m}$ . b, Velocity field of the membrane-bound beads (left) and the cytoplasmic beads (right) during the last 2 minutes of cellularization. c, The average displacement of beads along the AB axis plotted as a function of time. Only beads located within 15  $\mu\text{m}$  of the

ventral midline were included. The value  $x = 0$  is the onset of gastrulation;  $y = 0$  is the apical surface of the embryo. Blue arrows, average apical–basal displacement of beads within  $\Delta y = 2\text{-}\mu\text{m}$  and  $\Delta t = 30\text{-s}$  intervals. Red, streamlines. d, Velocity of beads along the AB axis during late cellularization ( $t = -8$  to 0 min) as a function of their initial depth at  $t = -8$  min. During the last 8 min of cellularization, the WGA beads show depth-dependent directional movement along the AB axis. Beads bound to the apical portion of the lateral membrane (approximately 0–10  $\mu\text{m}$ ) barely move. The velocity of beads below 15  $\mu\text{m}$  rapidly increases with depth and reaches a plateau of maximal velocity at 20  $\mu\text{m}$ , below which the beads move at the same, maximal speed. In contrast, the cytoplasmic beads do not undergo substantial movement during cellularization. Error bars, 95% confidence intervals.



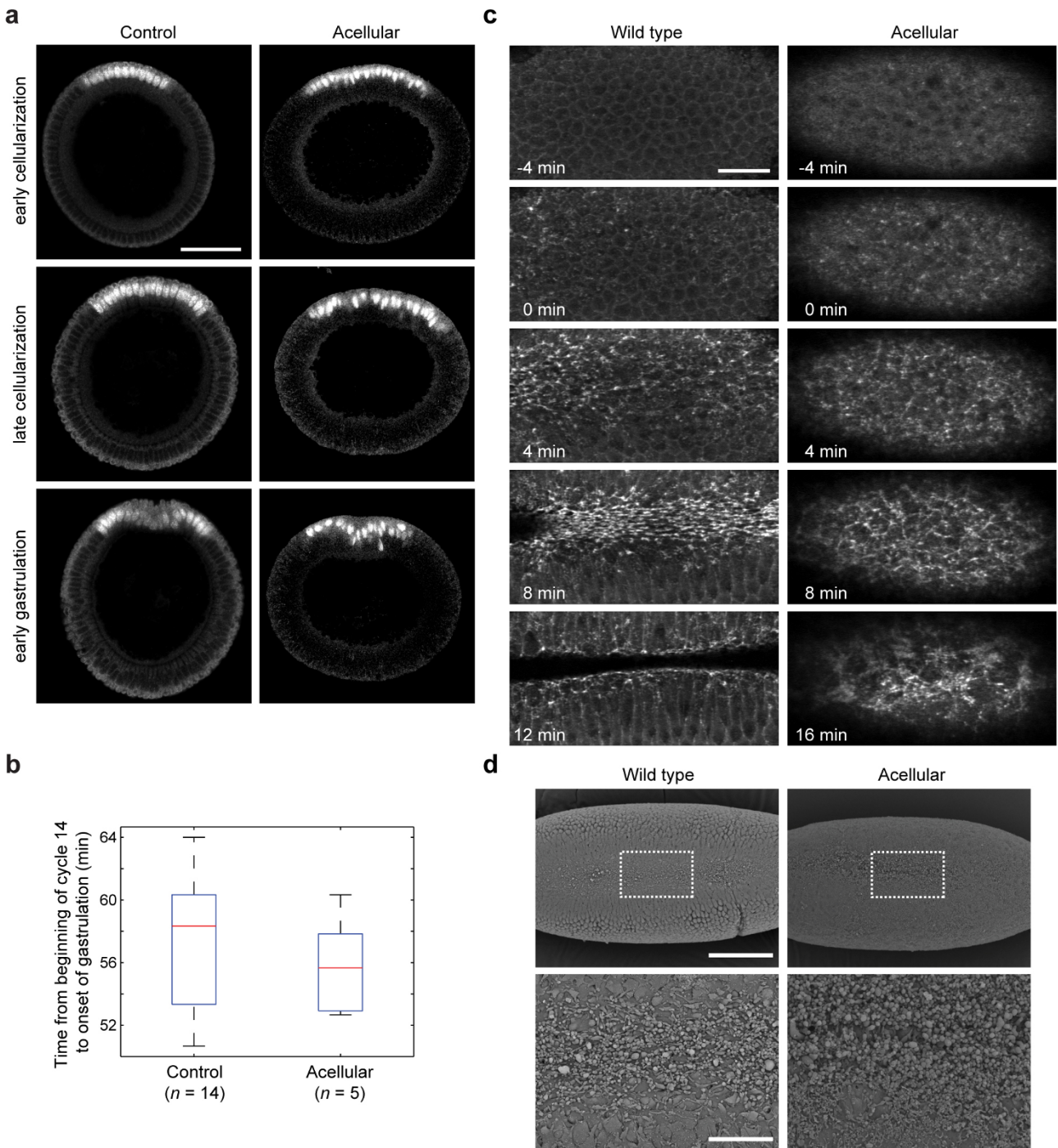
**Extended Data Figure 6 | Compensating the membrane flow for the impact of cellularization.** **a**, Difference ( $\Delta V = V_{\text{membrane}} - V_{\text{cytoplasm}}$ ) between the velocity fields of the membrane-bound beads and the cytoplasmic beads. Arrows indicate the velocity vectors of  $\Delta V$ , and the heat map corresponds to its magnitude. **b**, Generating velocity field that corresponds to residual cellularization. The resulting velocity field was subtracted from the corresponding membrane flow to compensate for the impact of cellularization

(Supplementary Methods). **c, d**, Streamlines of the membrane-bound beads (red) compared with the cytoplasmic beads (blue). The velocity field of the membrane-bound beads was either not compensated (**c**) or compensated (**d**) for cellularization. **e**, Average relative difference between the membrane flow and cytoplasmic flow before (blue) or after (red) compensating for the impact of residual cellularization. **f**, Average relative left-right difference of the velocity field.



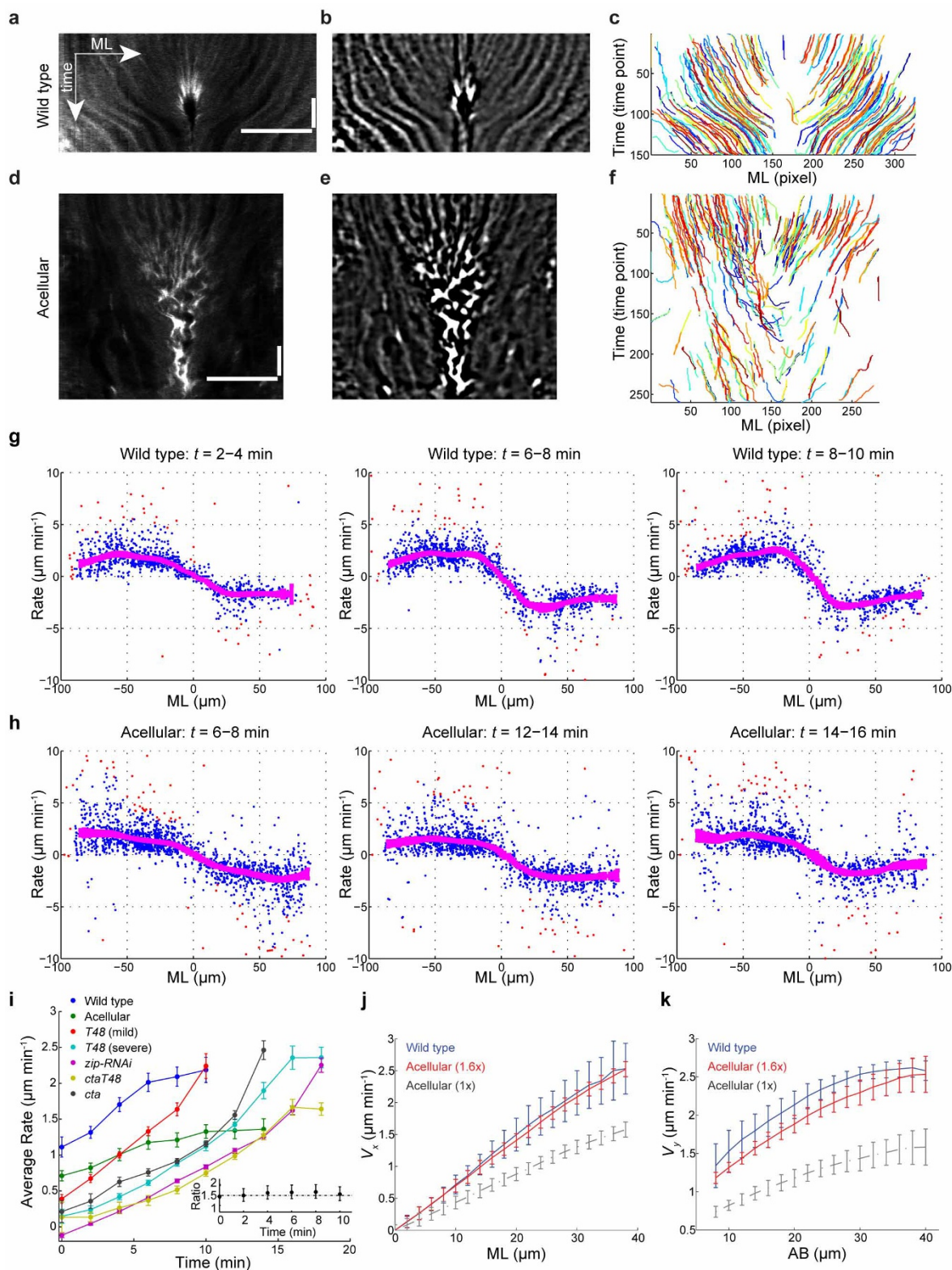
**Extended Data Figure 7 | The acellular embryos fail to form cells before gastrulation.** **a**, Time-lapse images of Sqh-GFP in the control or the acellular embryo imaged at the midsagittal plane. The control and acellular embryos are indistinguishable before cellularization. However, during cellularization, the acellular embryos only make very limited progress in membrane invagination. At the point when cellularization would normally be completed, only

discontinuous thread-like strands of membrane are formed extending 10–15  $\mu\text{m}$  into the cytoplasm; meanwhile the nuclei are still located in a common cytoplasm that is not partitioned into individual cells. Scale bar, 100  $\mu\text{m}$ . **b**, The wild-type and acellular embryos fixed during mid-cellularization and stained for membrane (Neurotactin, green) and myosin (Zipper, red). Scale bar, 50  $\mu\text{m}$ .



**Extended Data Figure 8 | The onset of gastrulation is normal in the acellular embryos.** **a**, Immunostaining of mesoderm determinant Snail in the acellular and control embryos fixed at early cellularization, late cellularization or early gastrulation. The pattern of Snail expression in the acellular embryos closely resembles that in the wild-type embryos. At early cycle 14, the Snail proteins are clearly detectable in the prospective mesoderm. The staining appears graded towards the mesoderm/ectoderm boundary at this stage. At mid-cycle 14 and early gastrulation, the staining becomes uniform across the entire prospective mesoderm. Scale bar, 50 µm. **b**, Quantification of duration between beginning of cycle 14 and the onset of gastrulation. On each box, the central

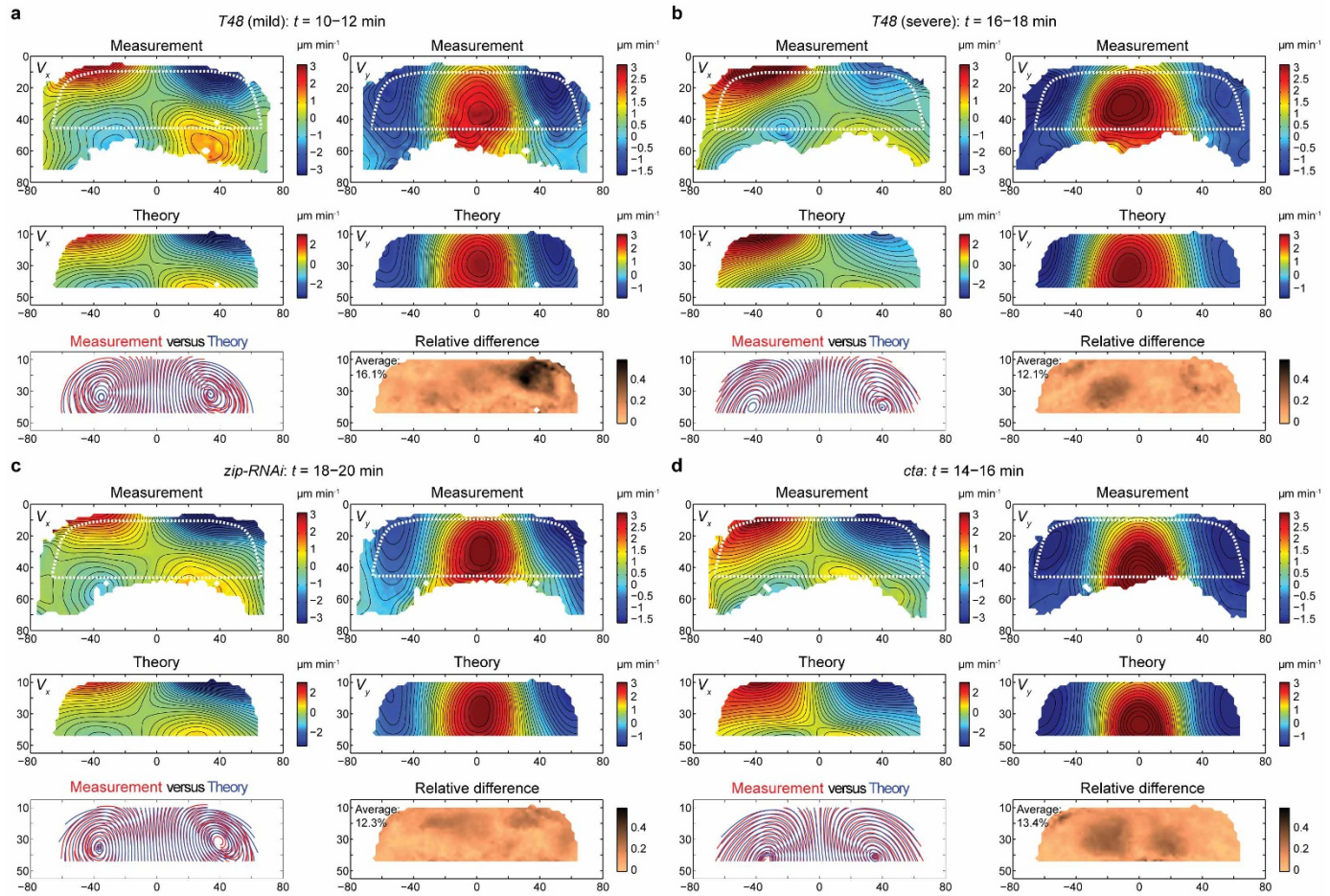
mark (red) is the median, the edges of the box are the 25th and 75th percentiles, and the whiskers extend to the most extreme data points not considered outliers. **c**, Apical myosin dynamics visualized using Sqh–GFP after the onset of gastrulation ( $t = 0$  min). Scale bar, 30 µm. **d**, Scanning electron microscope images showing the ventral surface of the wild-type and acellular embryos. Bottom panels show the enlarged view of the boxed regions in the top panels. Membrane blebs are formed in the ventral surface of the acellular embryos, indicating that apical constriction still gathers surface membrane into blebs despite the lack of cells. Scale bar, 50 µm (top); 10 µm (bottom).



#### Extended Data Figure 9 | Measuring the rate of apical constriction.

**a, d**, Kymograph of apical Sqh-GFP videos along the ML axis (compensated for the curvature of the embryos) demonstrating the movement of apical myosin towards the ventral midline. The x axis represents the ML axis; scale bar, 50  $\mu\text{m}$ ; the y axis represents time, scale bar, 5 min. **b, e**, Kymographs processed with a band-pass filter. **c, f**, Trajectories of apical myosin moving towards the ventral midline were tracked from the processed kymographs (showing results tracked from several kymographs). Colours are used to distinguish individual trajectories. **g, h**, The rate of apical constriction (that is, the rate of convergent movement of the apical cortex) at different times during

ventral furrow formation as a function of ML positions. The rate of apical constriction (magenta) was averaged from measurement of individual myosin trajectories over 2-min intervals (blue dots). Red dots are outliers. **i**, Average rate of apical constriction over time. For each time point, rates were averaged across the mid-ventral region ( $x = -50$  to 50  $\mu\text{m}$ ). Insert shows the ratio of rates between the wild-type and acellular embryos over time. Dashed line corresponds to 1.6 $\times$ . Error bars, s.e.m. **j**, Average  $V_x$  near the ventral cortex ( $y = 10$ –14  $\mu\text{m}$ ,  $t = 6$ –12 min) as a function of ML positions. **k**, Average  $V_y$  near the ventral midline ( $x = -16$  to 16  $\mu\text{m}$ ,  $t = 6$ –12 min) as a function of AB positions. Error bars, s.d. in **j** and **k**.



**Extended Data Figure 10 | Comparing the mutant flow profiles with the hydrodynamic predictions.** **a**, *T48* (mild),  $n = 5$  embryos; **b**, *T48* (severe),  $n = 6$  embryos; **c**, *zip-RNAi*,  $n = 10$  embryos; **d**, *cta*,  $n = 8$  embryos. For each mutant: top, heat maps of  $V_x$  and  $V_y$  (measurement); middle, heat maps of  $V_x$  and  $V_y$  (theoretical prediction); bottom left, streamlines of the measured

velocity field (red) compared with those deduced from the Stokes equations (blue); bottom right, relative difference between the measured velocity field and the hydrodynamic predictions. At the selected time points, the rate of apical constriction in each mutant is comparable to that in the wild type at  $t = 6\text{--}8$  min (Extended Data Fig. 9i).